Article

Reduced Silicon Fragmentation in Lithium Ion Battery Anodes using Electronic Doping Strategies

Derwin Lau, Charles Aram Hall, Sean Lim, Jodie A Yuwono, Patrick A Burr, Ning Song, and Alison Lennon

ACS Appl. Energy Mater., **Just Accepted Manuscript** • DOI: 10.1021/acsaem.9b02200 • Publication Date (Web): 23 Jan 2020

Reduced Silicon Fragmentation in Lithium Ion Battery Anodes using Electronic Doping Strategies

Authors: *Derwin Lau [a], Charles A. Hall [a], Sean Lim [b], Jodie A. Yuwono [a], Patrick A. Burr [c], Ning Song [a], Alison Lennon [a,*]*

[a] School of Photovoltaic and Renewable Energy Engineering, UNSW Sydney, NSW 2052, Australia

[b] The Electron Microscope Unit, UNSW Sydney, Sydney, 2052, Australia

[c] The School of Mechanical and Manufacturing Engineering, UNSW Sydney, NSW 2052, Australia

[*] Corresponding author: a.lennon@unsw.edu.au

Keyword: silicon anodes, lithium ion batteries, electronic doping, fragmentation, cycle life

ABSTRACT

Although Si anodes have the potential to achieve gravimetric capacities > 3000 mA g^{-1} for Li ion batteries, their utility has been limited by their large volumetric expansion on lithiation and electrode fragmentation. We show that n-type doping reduces the lithiation potential of (100) Si and conclude that the Li ion insertion energy into crystalline Si increases with n-type dopant density. This allows tuning of the n-type dopant density in Si electrodes to reduce surface fragmentation and increase electrode cycle life. Using a combination of n-type doping, prelithiation at a low current density of 0.05 mA cm^{-2} and areal capacity capping at 2 mAh cm^{-2}, we show that stable cycling can be achieved at a current density of 1 mA cm^{-2} within the potential range of 0.01–1.5 V for at least 140 cycles using an organic electrolyte without additives. Further improvements in cyclability can be achieved using alternative electrolytes with greater electrochemical stability at low potentials. Due to the massively reduced cost of Si wafers, heavily doped wafer-based current collectors may present an alternative to Si thin film anodes with improved adhesion between the current collector and electro-active Si surface provided that the wafers can be sufficiently thin to reduce electrode mass and volume. Alternatively, n-type doping of Si can be used to reduce fragmentation in particle-based electrodes permitting more controllable lithiation and longer cycle life.

1. INTRODUCTION

While Si anodes offer the promise of high theoretical capacity (3580 mAh g^{-1})[1–3] thick film Si electrodes typically have short cycle lives due to their large volume change upon lithiation (~280% for complete lithiation at ambient temperatures to the $Li_{3.75}Si$ phase).[1] The repetitive cycling with such high volumetric expansion co-efficient ultimately can ultimately lead to electrode fragmentation and eventual cycling failure.[4–6] Nanostructuring Si through the use of nanowires[7–10] or nanoparticles[11–15] can enhance electrode 'breathability'[12] to accommodate the volumetric expansion during lithiation, however it reduces electrode tapped density and can result in excessive solid electrolyte interphase (SEI) growth due to the large surface area exposed to the electrolyte.[16,17] This excessive and continuous growth of the SEI can then reduce capacity with cycling as the formed SEI continually breaks down during delithiation exposing a fresh Si surface for renewed SEI formation.[18]

Promising initial capacities of > 3000 mAh g^{-1} and capacity retentions of ~85% after 100 cycles have been reported for thin film amorphous Si (a-Si) films (t < 300 nm) with solid electrolytes being used to address the problems of excessive SEI growth.[19,20] However, these films have a low areal capacity of ~0.2 mAh cm^{-2}, which is much lower than the values typical for commercial Li-ion batteries (2–4 mAh cm^{-2})[21] and the capacity fades rapidly with the cycling of thicker films.[21,22] Sakabe et al. addressed this low mass loading limitation to some extent by using porous a-Si films (also with solid electrolytes). This porosity was introduced through the use of He as the sputtering gas rather than Ar.[21] With this strategy, they achieved a capacity retention of 93% at 100 cycles for films with a thickness of 1.55 μm and an areal capacity of 2.3 mAh cm^{-2}. In addition, the introduction of porosity did not impact the high-rate performance that has been observed for non-porous a-Si thin films, while also achieving an areal capacity of 1.2 mAh cm^{-2} at 3 C (1 C = 3.33 mA cm^{-2}).[21]

Another approach to address the capacity fade of a-Si thin films which was reported by Miyazaki et al. is to introduce O into the films during sputtering to form a Si-rich amorphous Si suboxide (a-SiO_x) films.[20] Although the suboxide reduces the discharge capacity at low rates (due to the O atoms not participating in the conversion reaction), cyclability was significantly increased due to a reduced resistance during cycling with a capacity retention of 99.94% in the first 100 cycles.[20] Miyazaki et al. proposed that the Si-O bonds present on the surface undergo reaction with Li in the early cycles to form a Li-O scaffold. Although the Li-O scaffold may not suppress the large volumetric changes that typically occur with cycling intrinsic a-Si thin film electrodes, it may minimise the increase in effective series resistance that is typically observed with cycling by immobilising Si atoms and reducing inhomogeneities of film thickness. Interestingly, it was shown that the Li-O scaffold did not impact the rate performance of the a-SiO_x electrode compared to that of pure a-Si and, at higher current densities of 5 and 10 mA cm^{-2}, the discharge capacities of the a-SiO_x and a-Si films were very similar.[20]

Film cracking with cycling may also be countered by increasing the electrical conductivity of Si as this can permit more uniform surface lithiation and minimise stress gradients.[11,23–25] A number of studies have investigated the role of dopants in Si in mitigating film fragmentation on cycling.[25–32] Most reports have focussed on crystalline Si (c-Si) due to its ability to be more readily modelled using density functional theory (DFT) approaches. Long et al. reported that the Li insertion potential shifts to lower voltages for P-doped and higher potential for B-doped (100) and (111) Si compared to intrinsic Si, due to the positive (less favourable) insertion energy for the P-doped c-Si and negative insertion energy for B-doped Si.[26] They attributed these differences in insertion energy to electronic effects (i.e., similar Li ion insertion energies were predicted for electron and hole-doped (100) and (111) Si as for P and B-doped Si, respectively). Long et al. also predicted, and then confirmed with Secondary Ion Mass Spectrometry (SIMS) measurements that for both B and P dopants there is a strong thermodynamic driving force for dopant atoms to segregate at the surface of (100) and (111) Si on lithiation and, in doing so, cause the effects of the different insertion potential to be greater than predicted from base doping levels.

McSweeney et al. confirmed the lower lithiation potential for n-type (100) Si and showed that Li ion insertion in n-type crystalline Si (c-Si) causes a conversion to a-Si after the first delithiation process,[27] similarly observed for intrinsic Si.[1–3] It was hypothesised in this study that the addition of n-type dopants could potentially minimise the excessive volume expansion that is typically responsible for the increased ohmic resistance on cycling. Furthermore, by tuning the dopant density and making the c-Si more conductive, Li may diffuse faster into the bulk in earlier cycles further reducing the volume expansion that occurs at the surface and preventing excessive fragmentation of the electrode.[11]

In this study, we investigated the effect of n-type dopant density on the capacity and cyclability of Si anodes using both experiments and density functional theory (DFT) modelling. Rather than depositing doped a-Si, as is performed in other studies,[23,28,33–35] we selected to pre-lithiate (100) polished Si wafer surfaces to form doped a-Si films while the remaining (100) Si was retained as the current collector for the electrode. It was hypothesised that this fabrication approach, which eliminates the need for a Cu foil-Si interface, may present some advantages with regard to resisting delamination of the active a-Si layer from the current collector[36–38] as amorphisation is expected to result in a rough, non-planar interface between the a-Si and c-Si current collector.[39] An improved understanding of the role of dopant element and density on lithiation/delithiation of Si anodes may also contribute to greater capacity retention with cycling for electrodes utilising micron-sized Si particles.

2. METHODS

2.1 Electrode fabrication

Silicon electrodes were fabricated using three different, double-side polished, n-type (100), 500 μm thick Si wafers (from Anhui Yisemi Semiconductor Co. Ltd): (i) 1–10 Ω cm As-doped, corresponding to a doping density between 4.4×10^{14}–4.8×10^{15} cm^{-3}; (ii) 0.01–0.05 Ω cm Sb-doped, corresponding to a doping density between 2.3×10^{17}–4.4×10^{18} cm^{-3}; and (iii) 0.001–0.005 Ω cm As-doped corresponding to a doping density between 1.2–7.4 × 10^{19} cm^{-3}.[40] The resistivity and base doping of the wafers were confirmed using Time-of-Flight Secondary Ion Mass Spectrometry (ToF SIMS) and a four-point probe measurements (see **Figure S1** and **Figure S2**).

The wafers were cleaved into 1 cm^2 square fragments before being cleaned using an RCA1 process[41] and immersed in 1:100 (v/v) 48 wt.% hydrofluoric acid (HF; Sigma Aldrich) DI water solution to remove any native surface SiO_x and H-terminate on the Si surface.[26] Wafer fragments were rinsed in DI water, then dried under N_2 and assembled into CR2032 coin cells with one polished Si wafer fragment surface in contact with the stainless steel plate of the coin cell assembly, a Celgard® 2325 Li-ion as separator film (17 mm diameter and 25 μm thick), 1 M $LiPF_6$ in 1:1 (v/v) ethylene carbonate (EC): ethyl methyl carbonate (EMC) (Sigma Aldrich) as electrolyte and a Li foil (Xiamen TMAX Li 16 mm diameter and 450 μm thick) as a counter electrode (see **Figure S3**). The volume of the electrolyte was 30 μL. Coin cell assembly was performed in a glove box (MBraun MB-LABStar 1250/780) in which H_2O and O_2 were maintained < 0.5 ppm.

2.2 Electrode characterisation

The fabricated coin cells were rested for 10 hrs before testing to ensure that the separators were fully impregnated with electrolyte. Selected coin cells from each dopant group were characterised using cyclic voltammetry (CV) using an IVIUM-n-Stat with sModule 2 A/20 V potentiostat. Cells with Si electrodes having the different doping densities were cycled from 3.0 to 0.01 V (*E* vs Li^+/Li) to confirm changes in lithiation potential with dopant element/density and cycling. All remaining coin cells were then prelithiated for 10 hrs unless otherwise specified from 3.0 towards 0.01 V at the current density of 0.05 mA cm^{-2} to form surface electro-active regions and enable stable cycling with high Coulombic efficiency (CE).[42] None of the electrodes reached the 0.01 V threshold during prelithiation due to the very low current density used for prelithiation. Upon reaching their respective prelithiation duration limits, they were immediately de-lithitated back to 3.0 V prior to further testing. This lithiation/delithiation cycle (cycle 0) is shown as the first data point for all galvanostatic charge-discharge (GCD) curves. All GCD tests were performed using a battery cycler (Neware BTS4000) within the potential range of 0.01 to 1.5 V (a typical *E* vs Li^+/Li potential window for Si anode)[5] at room temperature (25 °C).

After cycling, selected coin cells were opened in a glove box, rinsed thoroughly with dimethyl carbonate (DMC)[39] to remove organic salts and $LiPF_6$. Samples were then dried within the Ar rich glove box environment before being transferred to the imaging facility in an Ar-sealed container to minimise sample degradation and surface oxidation. Scanning electron microscope (SEM) images were obtained using a FEI NanoLab 450 while the cross-sections were milled using a focused-ion beam (FIB) FEI DualBeam NanoLab 200. Transmission electron microscope (TEM) electron beam diffraction images were acquired using a Phillip CM200 field transmission microscope. Selected area electron diffraction (SAED) patterns and TEM-EDX were used to identify the crystallinity and material composition from the high-resolution cross-sectional TEM images.

2.3 Density functional theory modelling

Plane-wave DFT calculations were implemented using the Vienna ab-initio simulation package (VASP),[43,44] with the core and valence electronic interactions being modelled using the projector augmented wave (PAW) method.[45,46] The exchange and correlation functional was described with the Perdew-Burke-Ernzerhof (PBE) functional.[47] Brillouin zone sampling was performed using the Monkhorst-Pack scheme with a k-point mesh of $7 \times 7 \times 7$ and a plane wave kinetic energy cut-off of 500 eV.

The obtained lattice parameter for a Si unit cell of 5.468 Å was consistent with previous DFT calculations using the PBE functional.[48] Supercells containing 64, 216, and 512 atoms of pristine and doped Si were constructed, with P, As and Sb introduced separately as single substitutional dopants to achieve the doping concentrations of 7.8×10^{20}, 2.31×10^{20} and 9.75×10^{19} cm^{-3}, respectively. Geometrical optimisations were achieved by relaxing all ionic positions and supercell vectors until the Hellman-Feynman forces were less than 0.01 eV/Å. Geometrical optimisations were achieved by relaxing all ionic positions and supercell vectors until the Hellman-Feynman forces were less than 0.01 eV/Å.

The influence of the dopant atom X (P, As, Sb) on the Li insertion enthalpy, was calculated by comparing the energy associated with accommodating Li in a doped Si crystal against that of accommodating Li in an intrinsic (undoped) Si crystal. The relative change in Li insertion enthalpy $\Delta E_{\mathrm{Li,insertion}}$, was calculated using:

$$\Delta E_{\text{Li, insertion}} = \frac{E_{\text{Li}_n\text{SiX}} - E_{\text{SiX}} - E_{\text{Li}_n\text{Si}} + E_{\text{Si}}}{n} \qquad \text{Eqn. (1)}$$

where $E_{\text{Li}_n\text{SiX}}$ and E_{SiX} are the DFT energies of the lithiated and delithiated X-doped crystalline Si supercell; $E_{\text{Li}_n\text{Si}}$ and E_{Si} are the DFT energies of the lithiated and delithiated intrinsic crystalline Si supercell (of supercell of the same size); and n is the number of Li atoms involved in the reaction.

3. Results and Discussion

3.1 Changes in lithiation potential with doping

Figure 1A shows the 1st CV cycle recorded at a scan rate of 1 mV s^{-1} for each of the doped Si electrodes prior to prelithiation (i.e., all electrodes were crystalline before being cycled). In this first scan, the peak lithiation current density was highest for the most lightly doped 1–10 Ω cm As-doped Si electrode (~235 μA cm^{-2}) and lowest for the most heavily doped 0.001–0.005 Ω cm As-doped Si electrode (~142 μA cm^{-2}). This observation is consistent with the hypothesis that lithiation becomes energetically less favourable with increased electron density or Si Fermi level as reported by Long et al.[26]

The lithiation onset potential was ~60 mV for all the Si electrodes in the 1st cycle (see **Figure 1A** inset). Lithiation below potentials of 50–70 mV has been shown to result in the formation of crystalline Li-rich $Li_{3.75}Si$ phase, even if the Si is amorphous at the start of the cycle.[3] This crystalline phase can induce high internal stresses due to its large volume expansion in the Si and can lead to delamination of the electro-active material and capacity fade.[28,49] In thin films, formation of $Li_{3.75}Si$ can be suppressed due to stresses induced by the presence of the current collector.[49] Domi et al. have also reported that P doping can inhibit the formation of this Li-rich crystalline phase due to the shrinking of the crystal lattice when P dopant atoms substitute Si atoms. They attributed the suppression of the Li-rich phase to the smaller increase in electrode thickness on lithiation and enhanced cycle life of electrodes (~1400 cycles with P doping compared with only ~600 cycles for intrinsic Si with an ionic liquid electrolyte).[28]

Delithiation of all the n-type doped Si electrodes occurred via the formation of two phases, which corresponds to peak current densities at the potentials of 348 and 535 mV in the first CV cycle (see **Figure 1A**). The potentials of these peaks were similar to values deduced by Schroder et al.[50] for intrinsic Si (290 and 490 mV), McSweeney et al. for 0.001–0.005 Ω cm As-doped (100) Si (~370 ~500 mV)[27] and Domi et al. P-doped amorphous Si (310 and 480 mV).[28] These peaks have been ascribed to the delithiation of the Li-rich ($Li_{3.5\text{-}3.75}Si$) and Li-poor ($Li_{2.33\text{-}2}Si$) phases, respectively[1,27,28] and have been associated with the formation of a-Si.[1] The delithiation peak potentials did not vary considerably with doping density, which is to be expected as the properties of the lithiated Si electrodes would be dominated by the inserted Li rather than the presence of dopant atoms. However, the ratio of the peak current due to delithiation of the Li-rich phase (321 mV peak for Cycle 1 in **Table S2**) compared to delithiation of the Li-poor phase (511 mV peak for Cycle 1 in **Table S2**) decreased from 1.23, 1.21 to 1.11 for the 1–10 Ω cm As-doped, 0.01–0.05 Ω cm Sb-doped and 0.001–0.005 Ω cm As-doped Si electrodes, respectively. This suggests that higher n-type doping concentration may suppress the formation of the Li-rich Si phase and thereby limit excessive volume expansion.

Domi et al. reported a similar suppression of the Li-rich Si phase and attributed this to a reduced lattice parameter arising from substitution Si atoms (atomic radius 0.111 nm) with smaller P dopant atoms (atomic radius 0.106 nm).[23,28] To investigate this effect further, we calculated the lattice spacing expected for the different dopant atoms and concentrations using DFT (see **Section 2.3**). **Figure 2A** shows the change in the lattice parameter of Si with increasing dopant density for the n-type dopants; P, As and Sb. The modelling results suggests that each dopant element has a different effect on the lattice constant of Si. While P-doping reduces the Si lattice constant as previously reported;[23,51] Sb and As have larger tetrahedral radii compared to Si and consequently result in increased lattice parameters.

To determine the effect of n-type dopant density on lithiation, we calculated the $\Delta E_{\text{Li,insertion}}$ for a Li ion inserted an increasing distance away from a dopant atom (P, As, and Sb). This represented a method of simulating the effect of reducing dopant density (assuming a homogeneous dopant distribution) since with lower dopant density there is a lower probability that a Li ion will be inserted close to a dopant atom. **Figure 2B** shows that the calculated $\Delta E_{\text{Li,insertion}}$ decreases as a function of distance from the dopant atom suggesting that the barrier to lithiation decreases with lower electronic doping for all dopant elements (i.e., it is not dependent on the dopant element or its size in the lattice). This DFT result can explain the trend of decreasing peak lithiation and delithiation currents with increased dopant density evident in the 1st CV cycle shown in **Figure 1A**. Only when the Li ion is inserted close to an n-type dopant is a larger $\Delta E_{\text{Li,insertion}}$ experienced, and as doping decreases to approach intrinsic Si an asymptotic $\Delta E_{\text{Li,insertion}}$ occurs. Interestingly, if the energetic barrier to lithiation was dominated by dopant atom size as suggested by Domi et al.,[23,28] then the smallest $\Delta E_{\text{Li,insertion}}$ would have been experienced by the 0.01–0.05 Ω cm Sb-doped Si electrode due to Si-Sb's larger tetrahedral radius. This does not appears be the case from the early lithiation stages presented in **Figure 1A** and **Figure 1B** (i.e., the 0.01–0.05 Ω cm Sb-doped Si does not have higher Li diffusion current or higher E vs Li^+/Li potential compare to other n-type Si investigated). This conclusion is consistent with the trend suggested by Long et al. using DFT calculations[26] and suggests that the barrier to lithiation may arise due to Coulombic interactions between the positively-charged Li ion and the ionised dopant atom. This simulation established that insertion energy may not be due to changes in the lattice parameter induced by dopant atoms that are smaller or larger than the Si atomic radius as suggested by Domi et al.[23,28] We propose instead that the $\Delta E_{\text{Li,insertion}}$ may depend primarily on the electronegativity of the dopant atom than its size. However, this theory will be further evaluated in future work.

The 2nd cycle lithiation CV curve for the electrodes (see **Figure 1B**) were clearly changed from those of the 1st cycle, with two lithiation peaks becoming evident. These corresponded (in terms of potential) to the two Si phases identified by Obrovac and Krause.[1] These lithiation peaks were also observed by McSweeney et al.[27] and provide further evidence to support the assumption that the Si surface regions of the wafers were amorphous after the 1st delithiation cycle. The lowest potential lithiation peak occurred at 189, 183 and 180 mV vs Li^+/Li for each of the 1–10 Ω cm As-doped, 0.01–0.05 Ω cm Sb-doped and 0.001–0.005 Ω cm As-doped Si electrodes, respectively (see **Figure S4**). This reflects the higher lithiation energy with increased dopant density even when the Si electrode is amorphous prior to lithiation. Furthermore, because this effect is observed in the absence of long-range crystal structure, it provides further evidence that crystal lattice effects due to dopant atom size are unlikely to be the basis for the increased Li ion insertion energy barrier that is observed for increasing n-type dopant density.[23]

Both the lithiation and delithiation peak current densities increased for all dopant densities upon further cycling and, after 50 cycles (see **Figure 1C**), currents were higher for the more heavily doped Si electrodes compared to the more lightly doped 1–10 Ω cm As-doped electrodes. This change in the peak current density trend may be due to the current becoming limited by wafer conductivity rather than the Li ion insertion energy. Dopant-mediated energy barriers to Li ion insertion may be reduced by the presence of an intermetallic silicide Li_xSi_y at the Si surface,[27] which would be expected to have a larger effect than the presence of dopant atoms. Additionally, only a single lithiation peak is evident after 50 cycles (see **Figure 1C**) and the delithiation peaks move to higher potential on cycling with the higher potential peak dominating the CV response. These potential changes in cycling were also observed by McSweeney et al.,[27] and suggest that a smaller fraction of lithiation current is due to the formation of the Li-rich phase of Li_xSi in later cycles. The increased lithiation currents may also be partly due to an increased Li ion diffusion coefficient which enables Li ions to penetrate further into the Si wafer to form Li-poor regions.[28] However, with increased cycling, it became difficult to separate the contributions of doping and wafer conductivity on the lithiation and delithiation currents.

On further cycling to 100 cycles (see **Figure 1D**), the peak delithiation current densities (see **Table S2**) of the lightly doped 1–10 Ω cm As-doped electrode were reduced from 161 μA cm^{-2} after 50 cycles to 59 μA cm^{-2} after 100 cycles. A small reduction in peak delithiation current density was also observed for the 0.01–0.05 Ω cm Sb-doped electrode (from 191 to 168 μA cm^{-2}) and no current density reduction was observed for the 0.001–0.005 Ω cm As-doped Si electrodes (peak delithiation current remained at 194 μA cm^{-2}). The reduced lithiation and delithiation peak current densities for the more lightly doped electrodes may indicate possible electrode degradation and highlights the need to investigate changes that are occurring at the surface of these Si wafer electrodes (see **Section 3.2**).

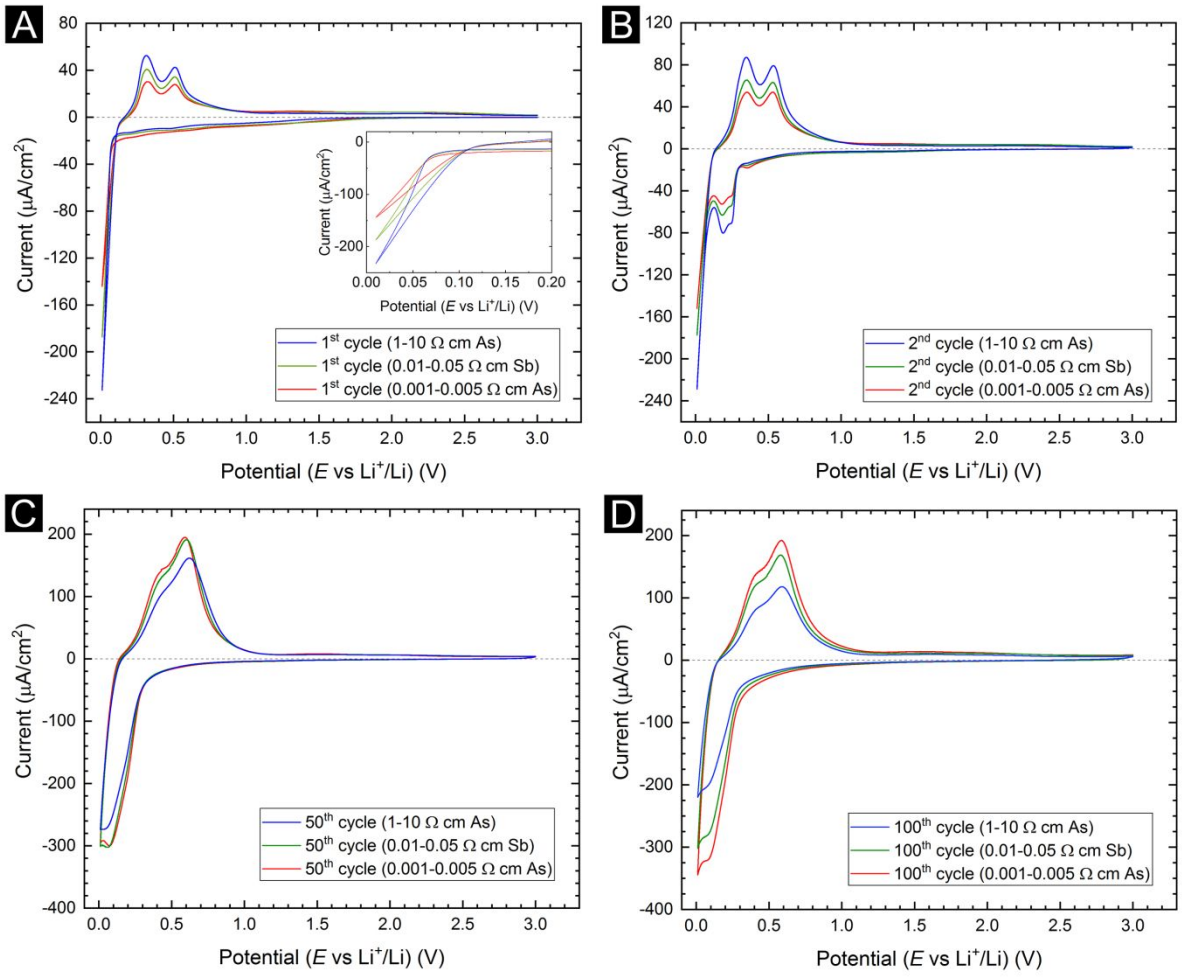

Figure 1: The 1st CV cycles **(A)**, 2nd CV cycles **(B)**, 50th CV cycles **(C)** and 100th CV cycles **(D)** for the n-type Si electrodes (no prelithiation) recorded at a scan rate of 1 mV s^{-1} from 0.01 to 3.0 V (*E* vs Li^+/Li). The inset graph in (A) shows a close-up of the current offset occurring < 60 mV for all Si electrodes. The peak current densities and potentials are tabulated in **Table S2** and **Table S3**.

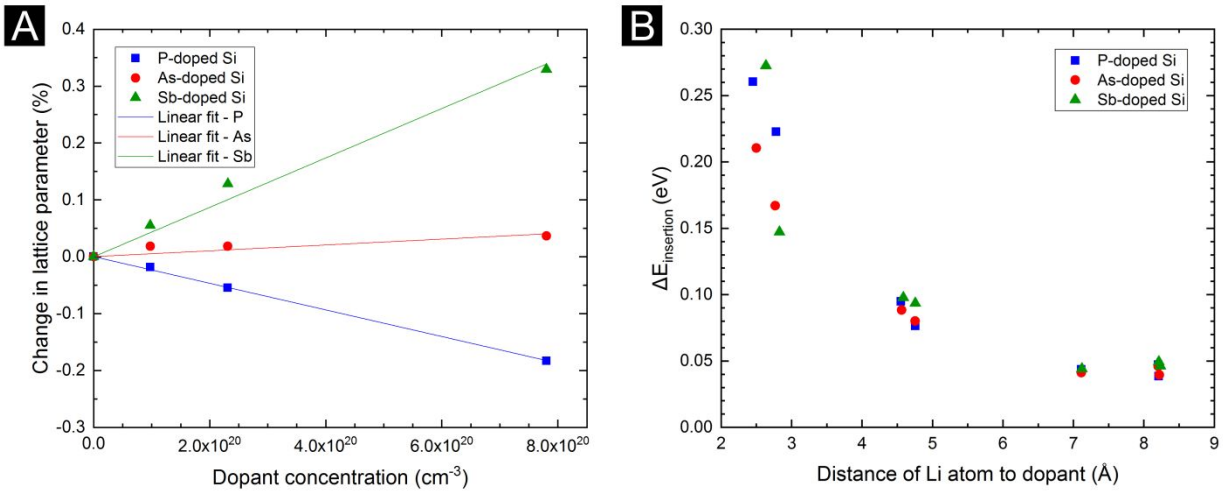

Figure 2: (A) Change in Si lattice parameter, computed using DFT, due to the introduction of P (■), As (●) and Sb (▲) dopants of increasing concentration into the crystalline Si lattice. **(B)** Relative change in Li insertion energy calculated for a Li ion inserted an increasing distance from a P, As or Sb dopant in a Si supercell comprising 216 atoms.

3.2 Surface morphology changes after prelithiation

Figure 3 shows SEM surface images of Si electrodes having different dopant densities from de-constructed coin cells after a prelithiation cycle at 0.05 mA cm^{-2} for 10, 20, 30 and 40 hrs and then delithiated to 3.0 V. Higher resolution images of selected regions are also shown in **Figure S5**. For all surfaces, cracks are evident on the Si surfaces and are indicative that a large volume expansion had occurred during prelithiation. Nanoscale differences in surface appearance in both figures may be due to a slight variation in the Si surface imaging preparation. For each dopant density, the extent of fragmentation increases with increased prelithiation duration. The cracks between fragments also appear to become wider and are more pronounced with prelithiation duration. The 1–10 Ω cm As-doped Si electrodes (see **Figure 3A-D**) displayed similar fragmentation patterns to those reported for thin intrinsic Si films,[52–54] which may suggest that low n-type dopant densities do not significantly affect the Si lithiation process.

Decreased surface fragmentation (corresponding to fragments of larger area) was evident with increased n-type dopant density for all lithiation durations. This is consistent with the higher dopant density presenting a larger initial barrier to Li ion insertion[26,27] and hence reduced volume expansion during prelithiation as observed by Domi et al.[28] Although the surfaces of the 0.01–0.05 Ω cm Sb-doped Si electrodes (see **Figure 3E-H**) resembled more closely the surfaces of the more heavily doped 0.001–0.005 Ω cm As-doped Si electrodes (see **Figure 3I-L**) for the shorter prelithiation durations, with longer prelithiation durations these electrodes eventually showed extensive cracking similar to the lightly doped 1–10 Ω cm As-doped electrodes for prelithiation durations of over 30 hrs.

Decreased surface fragmentation with increased doping density was also evident in the cross-sectional SEM images of the Si electrodes shown in **Figure 4**; which were recorded after 10 hrs of prelithiation. The surface fragments were smaller in area, thicker and more disconnected for the Si electrodes which were more lightly doped (see **Figure 4A** and **3B**). This implies greater induced strain and suggests that electrode failure due to loss of contact with the current collector may occur earlier than with the more heavily doped Si electrode (see **Figure 4C**). The thicker layers observed for the more lightly doped Si electrodes also appear to confirm that, at least during the early stages of prelithiation, Li ions penetrate more readily into the Si electrode's surfaces causing greater volumetric expansion. The increased conductivity of the more heavily doped Si electrodes may act to transport Li further into the Si with longer prelithiation durations and with increased cycling and this appears to be evident at the sites of cracks in the electrode surfaces (see **Figure S6**).

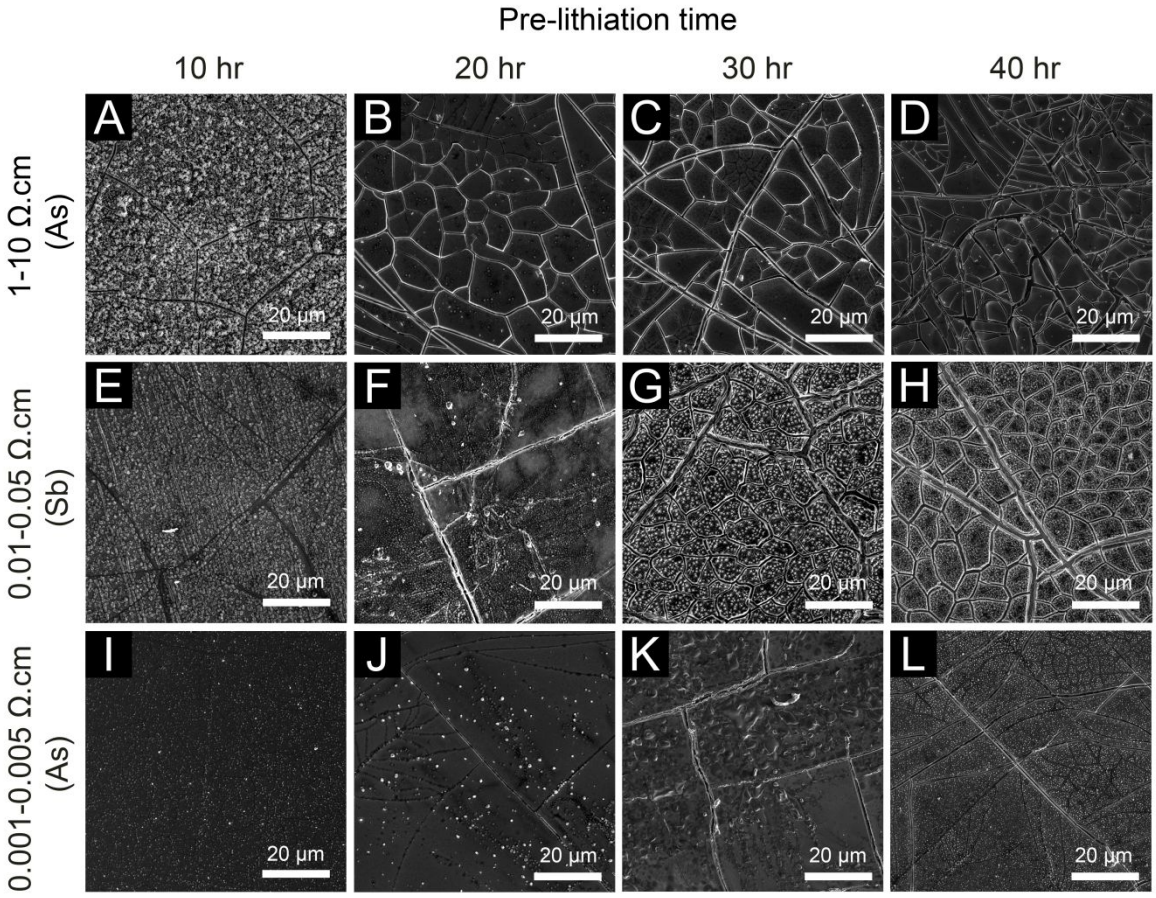

Figure 3: Scanning electron microscope images of the surfaces of selected 1–10 Ω cm As-doped **(A-D)**, 0.01–0.05 Ω cm Sb-doped **(E-H)** and 0.001–0.005 Ω cm As-doped **(I-L)** Si anode. Si electrodes with different dopant densities were imaged after being prelithiated at 0.05 mA cm^{-2} for 10, 20, 30 and 40 hrs and then delithiated at the same current density to 3.0 V. The coin cells were then opened in a glove box, rinsed thoroughly with DMC and maintained under Ar until imaged. Higher magnification SEM images of the same Si electrodes are available in **Figure S5**.

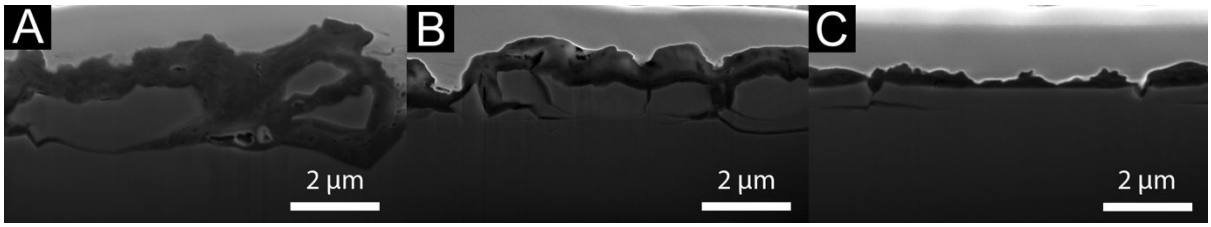

Figure 4: Cross-sectional SEM images recorded for selected 1–10 Ω cm As-doped (**A**), 0.01–0.05 Ω cm Sb-doped (**B**) and 0.001–0.005 Ω cm As-doped (**C**) Si electrodes which had been pre-lithitated for 10 hrs at 0.05 mA cm^{-2} and then discharged to 3.0 V prior to imaging. The surface of all electrodes was coated with Pt before imaging for increased conductivity.

As mentioned in **Section 3.1**, amorphisation of the crystalline Si after the first delithiation cycle has been reported for intrinsic Si[1,3,55,56] and n-type Si.[27] **Figure 5** shows TEM cross-sectional images with SAED images and TEM-EDX analysis for Si electrodes of different doping density after 10 hr of prelithiation at 0.05 mA cm^{-2}, and then discharged to 3.0 V prior to imaging. The SAED patterns for all Si electrodes confirm the amorphous nature of the surface fragment regions and the (110) crystal plane for each of the doped Si electrodes. Although the imaged surface fragment appears to have become completely separated from the Si wafer surface in places for the 0.01–0.05 Ω cm Sb-doped Si electrodes (see **Figure 5C-D**), for the other electrodes a dark boundary region appears between the a-Si surface region and the underlying crystalline Si wafer. This darker boundary region was not due to delamination of the fragments at least for the most heavily doped 0.001–0.005 Ω cm As-doped Si electrode as confirmed by the high-resolution TEM image shown in **Figure S8**.

The TEM-EDX images in **Figure 5B, D and F** identify an SEI layer which contains Si, O and Pt, Pt has been deposited to protect the surface from the Ga beam milling process. Closer inspection of the SAED results of the SEI regions revealed some bright spots which suggest the presence of crystallites within the amorphous layer. Further evidence for these polycrystalline regions is provided by the high-resolution TEM in **Figure S8** of a discharged 0.001–0.005 Ω cm As-doped Si electrode. Although the SEI that forms on Si anodes largely comprises products of reactions with the organic solvent and the PF_6^- ions (accounting for the presence of O and F elements in the EDX maps), Nie et al. also reported the possible formation of Li_xSiO_y and Li_xSiF_y in the SEI of Si electrodes.[57]

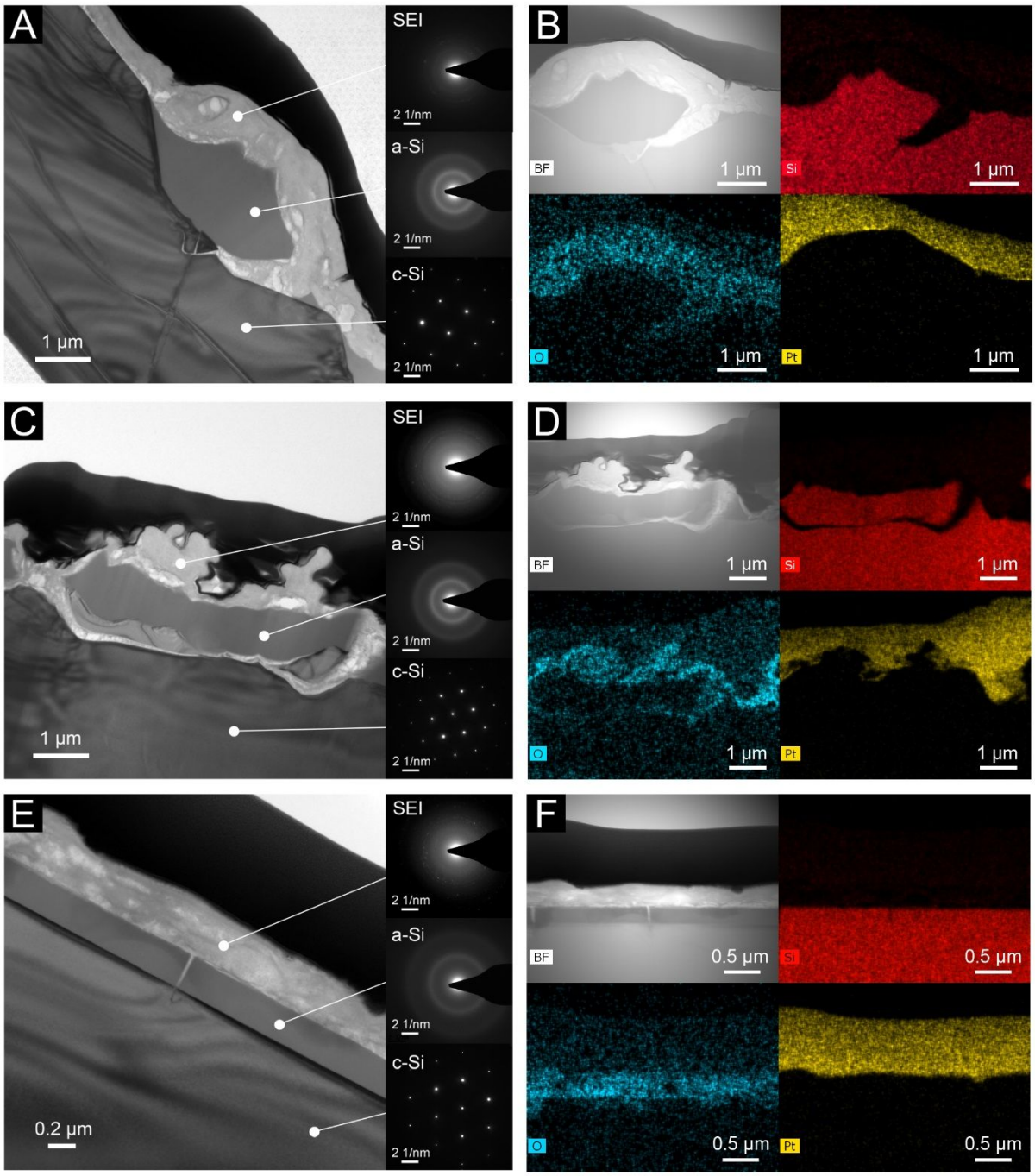

Figure 5: High resolution TEM cross-sectional images with SAED images (insets) and TEM-EDX analysis for Si electrodes of different doping density after prelithiation for 10 hr at 0.05 mA cm^{-2} and then discharging to 3.0 V prior to imaging; **(A-B)** 1–10 Ω cm As-doped, **(C-D)** 0.01–0.05 Ω cm Sb-doped and **(E-F)** 0.001–0.005 Ω cm As-doped Si electrodes.

3.3 Rate performance and cyclability

To explore the effect of n-type dopant density on the cyclability of the Si electrodes, coin cells were fabricated as described in **Section 2.2** and cycled at an incremental current density of 0.2 mA cm^{-2} from 0.4–2.0 mA cm^{-2} within the potential range of 0.01–1.5 V. All coin cells were prelithiated for 10 hrs as described in **Section 2.2.** To prevent excessive ongoing lithiation of the Si wafers (especially at the low current densities), the areal capacity of the coin cells was limited to 2 mAh cm^{-2} whilst cycling within the potential range of 0.01–1.5 V. Areal capacities were used rather than specific capacities (in mAh g^{-1}) in this analysis due to the difficulty in determining the mass of the electro-active Si. Given that the Si wafers acted both as a current collector and electro-active material, more Si may become lithiated with subsequent cycles. The extent of this addition lithiation with successive cycling is expected to vary for wafers of different conductivities. It should also be noted that after the prelithiation, the Si surfaces for all electrodes used for the rate performance and cyclability experiments reported in this section are assumed to be amorphous as shown in **Figure 5** and explained in **Section 3.2**.

Capacity capping is a strategy that has been frequently used to achieve stable Si anode cycling without excessive and continuing Si lithiation.[1,28,58] **Figure 6** shows lithiation/delithiation capacities and the CE for representative 1–10 Ω cm As-doped (blue), 0.01–0.05 Ω cm Sb-doped (green) and 0.001–0.005 Ω cm As-doped (red) Si electrodes. Representative GCD profiles for each current density and respective doping density are shown in **Figure S9**. All profiles exhibit a flat lithiation plateau in the charge/discharge curves < 1.0 V vs Li^+/Li and the onset of this plateau occurs at lower potential for the Si electrodes with higher dopant densities, which is consistent with their larger lithiation energy values.

The CE of the prelithiation cycle (Cycle 0) was similar for all electrodes irrespective of their doping (90.2– 95.3% for the 1–10 Ω cm As-doped, 88.7–94.1% for the 0.01–0.05 Ω cm Sb-doped and 91.0–95.8% for the 0.001–0.005 Ω cm As-doped Si electrodes, see **Figure S10A**). At current densities ≤ 0.8 mA cm^{-2}, all Si electrodes could attain the capped capacity of 2 mAh cm^{-2}. Their average CE over these initial cycles increased slightly and was less variable with increased doping density (99.3 ± 0.2% for the 1–10 Ω cm As-doped, 99.4 ± 0.1% for the 0.01–0.05 Ω cm Sb-doped and 99.7 ± 0.01% for the 0.001–0.005 Ω cm As-doped Si electrodes, see **Figure S10B**). This trend was presumably due to the more extensive surface fragmentation in the more lightly doped Si electrodes resulting in more electrolyte reactions as discussed in the previous section.

As the GCD current density was increased from 0.8 mA cm^{-2}, the 2 mAh cm^{-2} capacity limit was increasingly more difficult to achieve for the more lightly doped electrodes and the most heavily doped electrode retained the highest capacity at the higher rates (~0.7 mAh cm^{-2} at 2 mA cm^{-2}; see also **Figure S11**). The superior rate performance observed for the more heavily doped Si electrodes was attributed to lithiation (and delithiation) being increasingly limited by Si wafer conductivity at the higher rates since current must pass through the thickness of the wafer. It is also possible that the higher rate performance was due to a larger Li ion diffusion coefficient as reported by Domi et al. for their P-doped thin films on Cu.[28] The resistance experienced by the Si current collectors in the coin cells was more than three orders of magnitude greater for the 1–10 Ω cm As-doped electrodes compared to the 0.001–0.005 Ω cm As-doped Si electrodes (assuming uniform current flow across the electrode).

Interestingly, when all the Si electrodes were re-cycled at the final 0.4 mA cm^{-2}, the capped capacity of 2 mAh cm^{-2} was re-achieved (see **Figure 6**). Presumably at the higher rates, Li was only being inserted in the previously lithiated Si and no further electrode degradation was incurred. However, longer cycling at these faster rates may result in increased electrolyte decomposition and more extensive SEI formation due to higher overpotentials at the electrode surface. These results suggest that higher n-type dopant density can enable larger capacities at higher current densities (i.e., improved rate performance) for Si wafer-based electrodes. It should be noted that this higher rate performance for higher doping density may not be observed for electrodes comprising Si micro- or nanoparticles as capacity in these electrodes can be limited by the electrode composition (e.g., percentage of conductive C used in the slurry).

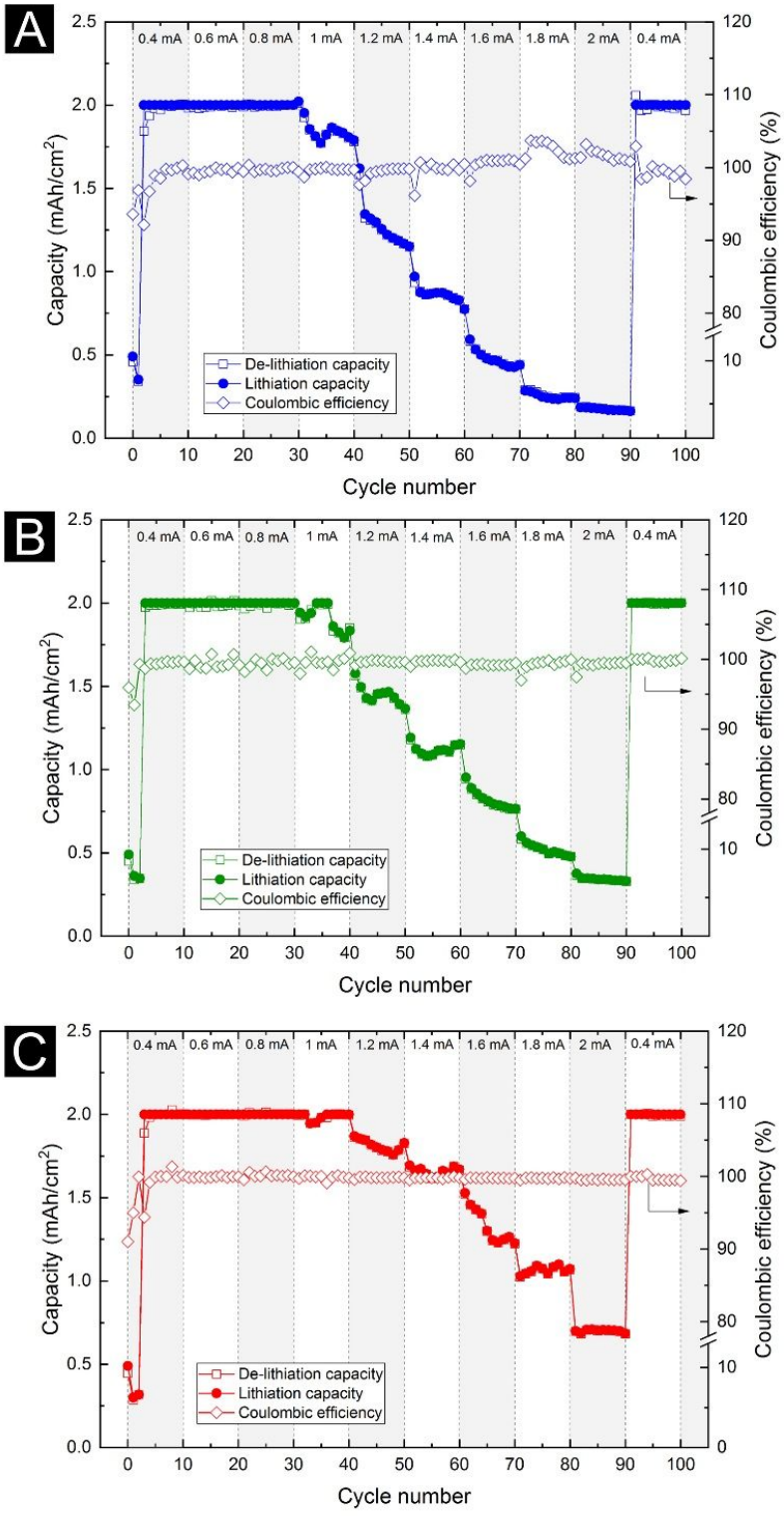

Figure 6: GCD lithiation (●) and delithiation (□) capacities and CE (◊) at different current densities for representative 1–10 Ω cm As-doped (A), 0.01–0.05 Ω cm Sb-doped (B) and 0.001–0.005 Ω cm As-doped (C) Si electrodes. All electrodes were prelithiated for 10 hrs at 0.05 mA cm^{-2}. During cycling the capacity of the coin cells was capped at a maximum capacity of 2 mAh cm^{-2} to prevent continuous lithiation of the Si wafer.

Figure 7 shows the lithiation/delithiation capacity and CE for representative prelithiated Si electrodes with different doping densities as a function of cycle number as the coin cells were cycled at 1 mA cm^{-2} between 0.01–1.5 V with a capped capacity of 2 mAh cm^{-2}. All electrodes followed a similar trend in the early cycles, first rapidly increasing, followed by a shallow decrease and then an increase in current with the two more heavily doped electrodes achieving the capped capacity within the first 50 cycles (see **Figure S12**). These changes occurred more rapidly for the 0.001–0.005 Ω cm As-doped Si electrodes, suggesting that wafer conductivity was limiting the achieved capacity in all cases. The most lightly doped electrode was not able to achieve the limiting capacity at the cycling current density used and reached a maximum capacity of ~1.60 mAh cm^{-2} before decaying rapidly to < 0.13 mAh cm^{-2} within the first 200 cycles.

The rapid increase in the capping capacity for the more heavily doped Si electrodes was assumed to be due to the lithiation front extending further into the Si wafers with each cycle, due to those wafers being more conductive than the 1–10 Ω cm As-doped wafers. Even higher capacities can be achieved at lower current densities. A similar increase in areal capacity for n-type Si electrodes was also reported by McSweeney et al. (see their manuscript's Fig. 9),[27] however their areal capacities were significantly lower than reported here due no prelithiation being performed before electrode cycling.

The use of capacity capping may have assisted in suppressing further Si fragmentation by limiting excessive lithiation and hence volumetric expansion.[28] The 1–10 Ω cm As-doped electrodes would have been more fragmented after the 10 hrs of prelithiation (see **Figure 4A**) and this may have contributed to their reduced cyclability as more electrolyte would presumably have been consumed in additional SEI formation. For the more conductive electrodes, if capping had not been applied, then continued lithiation would be expected to cause more volumetric expansion and hence surface fragmentation leading to reduced cyclability. While capacity capping could limit the volumetric expansion in this study, such methodology can present practical challenges since typically Li-ion cells capacity are determine by potential limits, such that they are charged at a constant current to a fixed voltage and then are held at a constant voltage until the current decreases to a certain value (CCCV charging).

The capacity of all electrodes eventually decayed to < 0.15 mAh cm^{-2} with the onset of this decay occurring after 80 and 120 cycles for the 0.01–0.05 Ω cm Sb-doped and 0.001–0.005 Ω cm As-doped (C) Si electrodes, respectively. The capacity fading in later cycles is likely due to electrode fragmentation and/or electrolyte decomposition. The CE of the 1–10 Ω cm As-doped electrodes became increasingly variable at the onset of the capacity fading, increasing to > 100% (see **Figure 7**) with some cycles indicating the occurrence of irreversible reactions. Superimposed on the lithiation reaction are the reactions associated with SEI formation due to electrolyte reduction, which is known to occur at potentials < 1.0 V.[39,59,60] As the electrolyte decomposes, the overpotential is expected to increase with increased SEI thickness and drive further electrolyte reduction reactions. These competing reactions are expected to occur for all the Si electrodes, however the lower conductivity of the 1–10 Ω cm As-doped electrodes is expected to result in higher overpotentials due to their lower conductivity, especially at higher current densities.

Although use of n-type doping and capacity capping can be used to achieve more stable cycling of Si electrodes, an electrolyte that is electrochemically stable at the low lithiation potentials on n-type Si will be required. Improved cyclability in thin film Si electrodes has been achieved using thiophosphate-based glasses (e.g., $80Li_2S.20P_2S_5$),[21] however it is challenging to achieve an intimate, low-resistance interface between these solid-state electrolytes and a rigid crystalline Si electrode. Domi et al.[28] have also shown that use of an ionic liquid electrolyte comprising 1 M Li bis(fluorosulfonyl)amide (LiFSA) in N-methyl-N-propylpyrrolidinium bis-(fluorosulfonyl)amide (Py13-FSA) can restrict the volume expansion of the Si during lithiation compared to that observed with an organic electrolyte.[28] Some decomposition compounds from the FSA anion were still observed on the surface after cycling, however small inorganic compounds such as LiF, which can form due to FSA decomposition, may act to improve the mechanical stability of the SEI by forming an ion-conducting passivation layer that prevents further electrolyte decomposition.[61–64] Interesting, Domi et al.[28] demonstrated that through P-doping of Si (100 ppm; estimated to be ~2.1×10^{18} cm^{-3} and equivalent to a resistivity of 0.015 Ω cm), use of a LiFSA/Py13-FSA electrolyte and capacity capping, stable cycling for at least 1400 cycles could be achieved using electrodes comprising 1.6 μm thick Si films formed on Cu current collector.

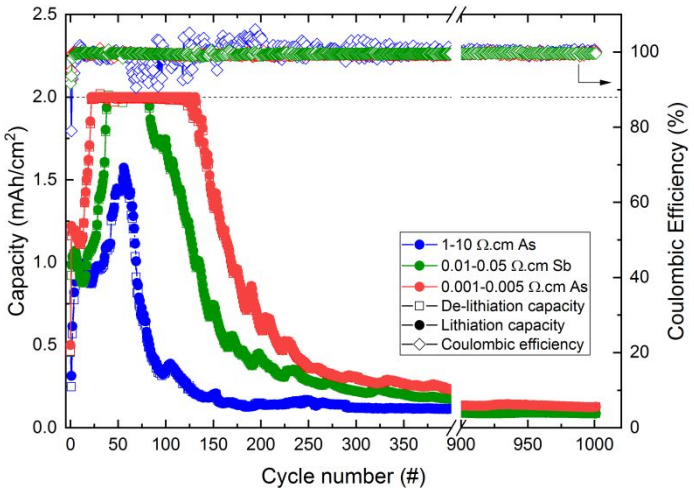

Figure 7: Lithiation/delithiation capacity and CE as a function of cycle number for representative 10 Ω cm As-doped (**blue**), 0.01–0.05 Ω cm Sb-doped (**green**) and 0.001–0.005 Ω cm As-doped (**red**) Si electrodes. All electrodes were prelithiated then cycled 1000 times at 1 mA cm^{-2} between 0.01–1.5 V with a capped capacity of 2 mAh cm^{-2}. An expanded view of the first 50 cycles can be found in the supporting information **Figure S12**.

The cost of Si wafers has reduced enormously due to large and rapid increases in Si photovoltaic manufacturing. This may permit a consideration of using heavily doped wafers as both the electroactive material and current collector for composite flat electrodes (e.g., as in pouch cells). These electrodes can reduce the need for conductive binders and metal foils and considerably simplify electrode fabrication. Additionally, the wafers provide a native interface between the electro-active material and current collector, which may enable strong adhesion and electrical contact due to minimal differences in the physical properties between the crystalline Si current collector and amorphous electro-active surface region. This stronger adhesion may assist in reducing electrode failures due to active material losing electrical contact with a Cu foil current collector.[36,37] However, heavily doped wafer-based Si electrodes will need to be substantially thinner (i.e., < 200 μm) than used in this study to reduce electrode mass and volume.[65] They will also require prelithiation and capacity capping in order to control deeper and uncontrollable lithiation into the Si crystal on continued cycling as demonstrated in **Figure 7**, especially if low charging rates are required. Problems associated with continued lithiation can potentially be avoided by use of higher rates, however these requirements will place larger demands on battery management systems. One possible application for these composite Si wafer electrodes may be hybrid devices where energy harvesting functionality (e.g., solar cell(s) for solar energy harvesting) is integrated with small-scale energy storage functionality to provide autonomous sources of power for devices such as sensors and implants.[66]

4. CONCLUSIONS

Our results demonstrate that surface fragmentation of Si electrodes can be reduced by introducing high densities of n-type dopants. This potential strategy for longer cycling Si anodes for Li ion batteries, which was also reported recently by Domi et al.,[28] is demonstrated using Si wafer electrodes as they allowed for a more detailed characterisation of the surface lithiation process and resulting fragmentation. The findings of this study have implications for thin film Si electrodes, comprising micro- and nanoparticle Si. In these cases, n-type doping can be employed to reduce particle fragmentation and loss of contact with a binder and/or current collector.

The reduced lithiation potential observed with n-type dopant density suggests that n-type doping increases the energy barrier to Li ion insertion into the Si crystal lattice and supresses the formation of Li-rich Li_xSi. This limits the volume of inserted Li and results in a thinner amorphous Si surface layer (after delithiation) with less surface fragmentation compared to Si electrodes with a lower n-type dopant density. Our results obtained from DFT modelling and experiments suggest that the observed increased barrier to lithiation is due primarily to electronic doping rather than changes in lattice spacing that occur with doping. The benefits of n-type doping for reduced surface fragmentation may be limited to early cycles because, once the Si surface is amorphous, the presence of residual Li in the Si is expected to overwhelm the contributions of electronic doping to Li insertion energy. In later cycles, lithiation becomes dominated by electrode conductivity and the lithiation currents of the more heavily doped electrodes surpass those in the more lightly doped electrodes.

The benefit of reduced volume expansion in early cycles by n-type doping needs to be balanced against the implications arising from the lower lithiation potential. This increases the likelihood of electrolyte decomposition upon subsequent cycling. Consequently, Si anodes employing electronic doping for reduced surface fragmentation will need to also consider the use of electrolyte additives that can assist with the formation of a stable SEI layer to minimise capacity fading or alternative solid-state/ionic liquid electrolytes.

Our results also highlight the possibility that heavily doped (conductive) Si wafers can potentially be used in place of Cu current collectors for some applications; but wafer thicknesses will need to be reduced appropriately to reduce resistive losses and electrode mass. Conductive Si wafers can provide a native interface between the active material and the current collector for stronger adhesion and electrical contact. This may assist in reducing electrode failures due to active material losing electrical contact with a Cu foil current collector. However, heavily doped wafer-based Si electrodes will require prelithiation and capacity capping in order to limit uncontrollable lithiation of the Si, especially if low charging rates are required. These requirements will place larger technical demands on battery management systems for safe and reliable cycling.

ACKNOWLEDGEMENT

The authors acknowledge the support of the AMMRF Microscopy Australia - UNSW Electron Microscope Unit, the UNSW School of Chemistry, the Australian Research Council through the Discovery Grant DP170103219 and Future Fellowship FT170100447 (Alison Lennon). Derwin Lau acknowledges receipt of a Research Training Scholarship provided by the Australian Government. Jodie A. Yuwono acknowledges the high-performance computational support from the Pawsey Supercomputing Centre and the National Computational Infrastructure, supported by Australian Government and the Government of Western Australia.

SUPPORTING INFORMATION

Additional methodology information and extended results for the manuscript can be found in the Supporting Information document.

REFERENCES

(1) Obrovac, M. N.; Krause, L. J. Reversible Cycling of Crystalline Silicon Powder. *J. Electrochem. Soc.* **2007**, *154* (2), A103.

(2) Key, B.; Morcrette, M.; Tarascon, J. M.; Grey, C. P. Pair Distribution Function Analysis and Solid State NMR Studies of Silicon Electrodes for Lithium Ion Batteries: Understanding the (de)Lithiation Mechanisms. *J. Am. Chem. Soc.* **2011**, *133* (3), 503–512.

(3) Obrovac, M. N.; Christensen, L. Structural Changes in Silicon Anodes during Lithium Insertion/Extraction. *Electrochem. Solid-State Lett.* **2004**, *7* (5), A93.

(4) Jin, Y.; Zhu, B.; Lu, Z.; Liu, N.; Zhu, J. Challenges and Recent Progress in the Development of Si Anodes for Lithium-Ion Battery. *Adv. Energy Mater.* **2017**, *7* (23), 1700715.

(5) Salah, M.; Murphy, P.; Hall, C.; Francis, C.; Kerr, R.; Fabretto, M. Pure Silicon Thin-Film Anodes for Lithium-Ion Batteries: A Review. *J. Power Sources* **2019**, *414*, 48–67.

(6) Ashuri, M.; He, Q.; Shaw, L. L. Silicon as a Potential Anode Material for Li-Ion Batteries: Where Size, Geometry and Structure Matter. *Nanoscale* **2016**, *8* (1), 74–103.

(7) Prosini, P. P.; Rufoloni, A.; Rondino, F.; Santoni, A. Silicon Nanowires Used as the Anode of a Lithium-Ion Battery. In *AIP Conference Proceedings*; 2015; Vol. 1667.

(8) Peng, K.; Jie, J.; Zhang, W.; Lee, S. T. Silicon Nanowires for Rechargeable Lithium-Ion Battery Anodes. *Appl. Phys. Lett.* **2008**, *93* (3), 033105.

(9) Chan, C. K.; Peng, H.; Liu, G.; McIlwrath, K.; Zhang, X. F.; Huggins, R. A.; Cui, Y. High-Performance Lithium Battery Anodes Using Silicon Nanowires. *Nat. Nanotechnol.* **2008**, *3* (1), 31–35.

(10) Zamfir, M. R.; Nguyen, H. T.; Moyen, E.; Lee, Y. H.; Pribat, D. Silicon Nanowires for Li-Based Battery Anodes: A Review. *Journal of Materials Chemistry A*. 2013, pp 9566–9586.

(11) Szczech, J. R.; Jin, S. Nanostructured Silicon for High Capacity Lithium Battery Anodes. *Energy Environ. Sci.* **2011**, *4* (1), 56–72.

(12) Liu, N.; Lu, Z.; Zhao, J.; Mcdowell, M. T.; Lee, H. W.; Zhao, W.; Cui, Y. A Pomegranate-Inspired Nanoscale Design for Large-Volume-Change Lithium Battery Anodes. *Nat. Nanotechnol.* **2014**, *9* (3), 187–192.

(13) Liu, X. H.; Zhong, L.; Huang, S.; Mao, S. X.; Zhu, T.; Huang, J. Y. Size-Dependent Fracture of Silicon Nanoparticles during Lithiation. *ACS Nano* **2012**, *6* (2), 1522–1531.

(14) McDowell, M. T.; Ryu, I.; Lee, S. W.; Wang, C.; Nix, W. D.; Cui, Y. Studying the Kinetics of Crystalline Silicon Nanoparticle Lithiation with in Situ Transmission Electron Microscopy. *Adv. Mater.* **2012**, *24* (45), 6034–6041.

(15) Obrovac, M. N.; Chevrier, V. L. Alloy Negative Electrodes for Li-Ion Batteries. *Chemical Reviews*. American Chemical Society December 10, 2014, pp 11444–11502.

(16) Lin, D.; Lu, Z.; Hsu, P. C.; Lee, H. R.; Liu, N.; Zhao, J.; Wang, H.; Liu, C.; Cui, Y. A High Tap Density Secondary Silicon Particle Anode Fabricated by Scalable Mechanical Pressing for Lithium-Ion Batteries. *Energy Environ. Sci.* **2015**, *8* (8), 2371–2376.

(17) Shi, F.; Song, Z.; Ross, P. N.; Somorjai, G. A.; Ritchie, R. O.; Komvopoulos, K. Failure Mechanisms of Single-Crystal Silicon Electrodes in Lithium-Ion Batteries. *Nat. Commun.* **2016**, *7*, 11886.

(18) Rahman, M. A.; Song, G.; Bhatt, A. I.; Wong, Y. C.; Wen, C. Nanostructured Silicon Anodes for High-Performance Lithium-Ion Batteries. *Adv. Funct. Mater.* **2016**, *26* (5), 647–678.

(19) Miyazaki, R.; Ohta, N.; Ohnishi, T.; Sakaguchi, I.; Takada, K. An Amorphous Si Film Anode for All-Solid-State Lithium Batteries. *J. Power Sources* **2014**, *272*, 541–545.

(20) Miyazaki, R.; Ohta, N.; Ohnishi, T.; Takada, K. Anode Properties of Silicon-Rich Amorphous Silicon Suboxide Films in All-Solid-State Lithium Batteries. *J. Power Sources* **2016**, *329*, 41–49.

(21) Sakabe, J.; Ohta, N.; Ohnishi, T.; Mitsuishi, K.; Takada, K. Porous Amorphous Silicon Film Anodes for High-Capacity and Stable All-Solid-State Lithium Batteries. *Commun. Chem.*

2018, *1* (1), 24.

(22) Maranchi, J. P.; Hepp, A. F.; Kumta, P. N. High Capacity, Reversible Silicon Thin-Film Anodes for Lithium-Ion Batteries. *Electrochem. Solid-State Lett.* **2003**, *6* (9), A198.

(23) Domi, Y.; Usui, H.; Shimizu, M.; Kakimoto, Y.; Sakaguchi, H. Effect of Phosphorus-Doping on Electrochemical Performance of Silicon Negative Electrodes in Lithium-Ion Batteries. *ACS Appl. Mater. Interfaces* **2016**, *8* (11), 7125–7132.

(24) Domi, Y.; Usui, H.; Narita, M.; Fujita, Y.; Yamaguchi, K.; Sakaguchi, H. Advanced Performance of Annealed Ni–P/(Etched Si) Negative Electrodes for Lithium–Ion Batteries. *J. Electrochem. Soc.* **2017**, *164* (13), A3208–A3213.

(25) Ge, M.; Rong, J.; Fang, X.; Zhou, C. Porous Doped Silicon Nanowires for Lithium Ion Battery Anode with Long Cycle Life. *Nano Lett.* **2012**, *12* (5), 2318–2323.

(26) Long, B. R.; Chan, M. K. Y.; Greeley, J. P.; Gewirth, A. A. Dopant Modulated Li Insertion in Si for Battery Anodes: Theory and Experiment. *J. Phys. Chem. C* **2011**, *115* (38), 18916–18921.

(27) McSweeney, W.; Lotty, O.; Glynn, C.; Geaney, H.; Holmes, J. D.; O'Dwyer, C. The Influence of Carrier Density and Doping Type on Lithium Insertion and Extraction Processes at Silicon Surfaces. *Electrochim. Acta* **2014**, *135*, 356–367.

(28) Domi, Y.; Usui, H.; Yamaguchi, K.; Yodoya, S.; Sakaguchi, H. Silicon-Based Anodes with Long Cycle Life for Lithium-Ion Batteries Achieved by Significant Suppression of Their Volume Expansion in Ionic-Liquid Electrolyte. *ACS Appl. Mater. Interfaces* **2019**, *11* (3), 2950–2960.

(29) Rousselot, S.; Gauthier, M.; Mazouzi, D.; Lestriez, B.; Guyomard, D.; Roué, L. Synthesis of Boron-Doped Si Particles by Ball Milling and Application in Li-Ion Batteries. *J. Power Sources* **2012**, *202*, 262–268.

(30) Yi, R.; Zai, J.; Dai, F.; Gordin, M. L.; Wang, D. Improved Rate Capability of Si-C Composite Anodes by Boron Doping for Lithium-Ion Batteries. *Electrochem. commun.*

2013, *36*, 29–32.

(31) Chen, X.; Gerasopoulos, K.; Guo, J.; Brown, A.; Ghodssi, R.; Culver, J. N.; Wang, C. High Rate Performance of Virus Enabled 3D N-Type Si Anodes for Lithium-Ion Batteries. *Electrochim. Acta* **2011**, *56* (14), 5210–5213.

(32) Lee, M.; Yoon, D.; Lee, U. J.; Umirov, N.; Mukanova, A.; Bakenov, Z.; Kim, S. S. The Electrochemical Performances of N-Type Extended Lattice Spaced Si Negative Electrodes for Lithium-Ion Batteries. *Front. Chem.* **2019**, *7* (May), 389.

(33) Mukanova, A.; Nurpeissova, A.; Kim, S. S.; Myronov, M.; Bakenov, Z. N-Type Doped Silicon Thin Film on a Porous Cu Current Collector as the Negative Electrode for Li-Ion Batteries. *ChemistryOpen* **2018**, *7* (1), 92–96.

(34) Arie, A. A.; Lee, J. K. Electrochemical Properties of P-Doped Silicon Thin Film Anodes of Lithium Ion Batteries. *Mater. Sci. Forum* **2013**, *737*, 80–84.

(35) Song, J. O.; Shim, H. T.; Byun, D. J.; Lee, J. K. A Study on the Effect of Structure and P-Doping of Si Thin Film as an Anode for Lithium Rechargeable Batteries. *Solid State Phenom.* **2007**, *124–126*, 1063–1066.

(36) Pal, S.; Damle, S. S.; Kumta, P. N.; Maiti, S. Modeling of Lithium Segregation Induced Delamination of A-Si Thin Film Anode in Li-Ion Batteries. *Comput. Mater. Sci.* **2013**, *79*, 877–887.

(37) Stournara, M. E.; Xiao, X.; Qi, Y.; Johari, P.; Lu, P.; Sheldon, B. W.; Gao, H.; Shenoy, V. B. Li Segregation Induces Structure and Strength Changes at the Amorphous Si/Cu Interface. *Nano Lett.* **2013**, *13* (10), 4759–4768.

(38) Sethuraman, V. A.; Chon, M. J.; Shimshak, M.; Srinivasan, V.; Guduru, P. R. In Situ Measurements of Stress Evolution in Silicon Thin Films during Electrochemical Lithiation and Delithiation. *J. Power Sources* **2010**, *195* (15), 5062–5066.

(39) Lee, Y. M.; Lee, J. Y.; Shim, H.-T.; Lee, J. K.; Park, J.-K. SEI Layer Formation on Amorphous Si Thin Electrode during Precycling. *J. Electrochem. Soc.* **2007**, *154* (6), A515.

(40) SIEGERT WAFER GmbH. Resistivity Calculator https://www.siegertwafer.com/calculator.html (accessed Aug 1, 2019).

(41) Bachman, M. RCA-1 Silicon Wafer Cleaning. *INRF Appl. note, UCI Integr. Nanosyst. Res. Facil.* **1999**, 1–3.

(42) Domi, Y.; Usui, H.; Iwanari, D.; Sakaguchi, H. Effect of Mechanical Pre-Lithiation on Electrochemical Performance of Silicon Negative Electrode for Lithium-Ion Batteries. *J. Electrochem. Soc.* **2017**, *164* (7), A1651–A1654.

(43) Kresse, G.; Furthmüller, J. Efficiency of Ab-Initio Total Energy Calculations for Metals and Semiconductors Using a Plane-Wave Basis Set. *Comput. Mater. Sci.* **1996**, *6* (1), 15–50.

(44) Kresse, G.; Furthmüller, J. Efficient Iterative Schemes for Ab Initio Total-Energy Calculations Using a Plane-Wave Basis Set. *Phys. Rev. B - Condens. Matter Mater. Phys.* **1996**, *54* (16), 11169–11186.

(45) Blöchl, P. E. Projector Augmented-Wave Method. *Phys. Rev. B* **1994**, *50* (24), 17953–17979.

(46) Kresse, G.; Joubert, D. From Ultrasoft Pseudopotentials to the Projector Augmented-Wave Method. *Phys. Rev. B - Condens. Matter Mater. Phys.* **1999**, *59* (3), 1758–1775.

(47) Perdew, J. P.; Burke, K.; Ernzerhof, M. Generalized Gradient Approximation Made Simple. *Phys. Rev. Lett.* **1996**, *77* (18), 3865–3868.

(48) He, L.; Liu, F.; Hautier, G.; Oliveira, M. J. T.; Marques, M. A. L.; Vila, F. D.; Rehr, J. J.; Rignanese, G. M.; Zhou, A. Accuracy of Generalized Gradient Approximation Functionals for Density-Functional Perturbation Theory Calculations. *Phys. Rev. B - Condens. Matter Mater. Phys.* **2014**, *89* (6), 064305.

(49) Iaboni, D. S. M.; Obrovac, M. N. Li15Si4 Formation in Silicon Thin Film Negative Electrodes. *J. Electrochem. Soc.* **2016**, *163* (2), A255–A261.

(50) Schroder, K. W.; Celio, H.; Webb, L. J.; Stevenson, K. J. Examining Solid Electrolyte Interphase Formation on Crystalline Silicon Electrodes: Influence of Electrochemical Preparation and Ambient Exposure Conditions. *J. Phys. Chem. C* **2012**, *116* (37), 19737–19747.

(51) Celotti, G.; Nobili, D.; Ostoja, P. Lattice Parameter Study of Silicon Uniformly Doped with Boron and Phosphorus. *J. Mater. Sci.* **1974**, *9* (5), 821–828.

(52) Li, J.; Dozier, A. K.; Li, Y.; Yang, F.; Cheng, Y.-T. Crack Pattern Formation in Thin Film Lithium-Ion Battery Electrodes. *J. Electrochem. Soc.* **2011**, *158* (6), A689.

(53) Maranchi, J. P.; Hepp, A. F.; Evans, A. G.; Nuhfer, N. T.; Kumta, P. N. Interfacial Properties of the A-SiCu: Active-Inactive Thin-Film Anode System for Lithium-Ion Batteries. *J. Electrochem. Soc.* **2006**, *153* (6), A1246.

(54) Baggetto, L.; Niessen, R. A. H.; Roozehoom, F.; Notten, P. H. L. High Energy Density All-Solid-State Batteries: A Challenging Concept towards 3D Integration. *Adv. Funct. Mater.* **2008**, *18* (7), 1057–1066.

(55) Limthongkul, P.; Jang, Y. Il; Dudney, N. J.; Chiang, Y. M. Electrochemically-Driven Solid-State Amorphization in Lithium-Silicon Alloys and Implications for Lithium Storage. *Acta Mater.* **2003**, *51* (4), 1103–1113.

(56) Li, H.; Huang, X.; Chen, L.; Zhou, G.; Zhang, Z.; Yu, D.; Jun Mo, Y.; Pei, N. Crystal Structural Evolution of Nano-Si Anode Caused by Lithium Insertion and Extraction at Room Temperature. *Solid State Ionics* **2000**, *135* (1–4), 181–191.

(57) Nie, M.; Abraham, D. P.; Chen, Y.; Bose, A.; Lucht, B. L. Silicon Solid Electrolyte Interphase (SEI) of Lithium Ion Battery Characterized by Microscopy and Spectroscopy. *J. Phys. Chem. C* **2013**, *117* (26), 13403–13412.

(58) Liu, W.-R.; Yang, M.-H.; Wu, H.-C.; Chiao, S. M.; Wu, N.-L. Enhanced Cycle Life of Si Anode for Li-Ion Batteries by Using Modified Elastomeric Binder. *Electrochem. Solid-State Lett.* **2005**, *8* (2), A100.

(59) Cheng, X. B.; Zhang, R.; Zhao, C. Z.; Wei, F.; Zhang, J. G.; Zhang, Q. A Review of Solid Electrolyte Interphases on Lithium Metal Anode. *Adv. Sci.* **2015**, *3*, 1500213.

(60) Pereira-Nabais, C.; Światowska, J.; Rosso, M.; Ozanam, F.; Seyeux, A.; Gohier, A.; Tran-Van, P.; Cassir, M.; Marcus, P. Effect of Lithiation Potential and Cycling on Chemical and Morphological Evolution of Si Thin Film Electrode Studied by ToF-SIMS. *ACS Appl. Mater. Interfaces* **2014**, *6* (15), 13023–13033.

(61) Piper, D. M.; Evans, T.; Leung, K.; Watkins, T.; Olson, J.; Kim, S. C.; Han, S. S.; Bhat, V.; Oh, K. H.; Buttry, D. A.; Lee, S. H. Stable Silicon-Ionic Liquid Interface for next-Generation Lithium-Ion Batteries. *Nat. Commun.* **2015**, *6*, 6230.

(62) Budi, A.; Basile, A.; Opletal, G.; Hollenkamp, A. F.; Best, A. S.; Rees, R. J.; Bhatt, A. I.; O'Mullane, A. P.; Russo, S. P. Study of the Initial Stage of Solid Electrolyte Interphase Formation upon Chemical Reaction of Lithium Metal and N -Methyl- N -Propyl-Pyrrolidinium- Bis(Fluorosulfonyl)Imide. *J. Phys. Chem. C* **2012**, *116* (37), 19789–19797.

(63) Shkrob, I. A.; Marin, T. W.; Zhu, Y.; Abraham, D. P. Why Bis(Fluorosulfonyl)Imide Is a "Magic Anion" for Electrochemistry. *J. Phys. Chem. C* **2014**, *118* (34), 19661–19671.

(64) Philippe, B.; Dedryvèire, R.; Gorgoi, M.; Rensmo, H.; Gonbeau, D.; Edström, K. Improved Performances of Nanosilicon Electrodes Using the Salt LiFSI: A Photoelectron Spectroscopy Study. *J. Am. Chem. Soc.* **2013**, *135* (26), 9829–9842.

(65) Eftekhari, A. On the Theoretical Capacity/Energy of Lithium Batteries and Their Counterparts. *ACS Sustain. Chem. Eng.* **2019**, *7* (4), 3684–3687.

(66) Lau, D.; Song, N.; Hall, C.; Jiang, Y.; Lim, S.; Perez-Wurfl, I.; Ouyang, Z.; Lennon, A. Hybrid Solar Energy Harvesting and Storage Devices: The Promises and Challenges. *Materials Today Energy*. Elsevier September 1, 2019, pp 22–44.

Insert Table of Contents artwork here

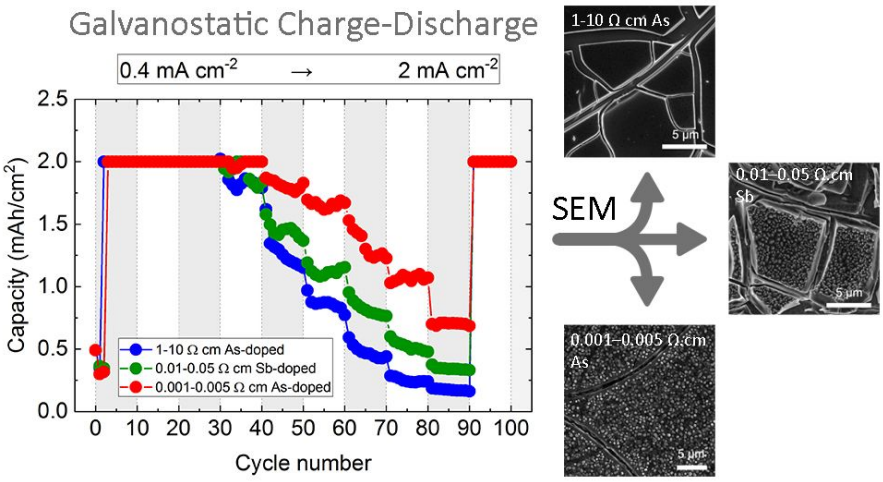

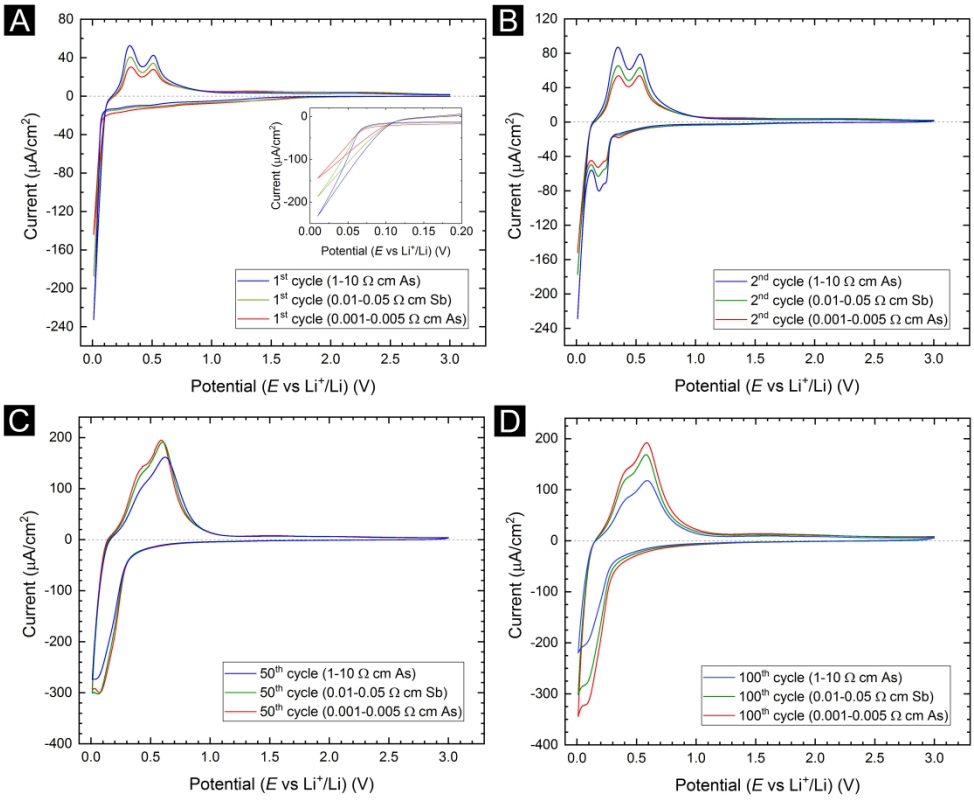

Figure 1: The 1st CV cycles (A), 2nd CV cycles (B), 50th CV cycles (C) and 100th CV cycles (D) for the n-type Si electrodes (no prelithiation) recorded at a scan rate of 1 mV s^{-1} from 0.01 to 3.0 V (*E* vs Li^+/Li). The inset graph in (A) shows a close-up of the current offset occurring < 60 mV for all Si electrodes. The peak current densities and potentials are tabulated in Table S2 and Table S3.

458x370mm (300 x 300 DPI)

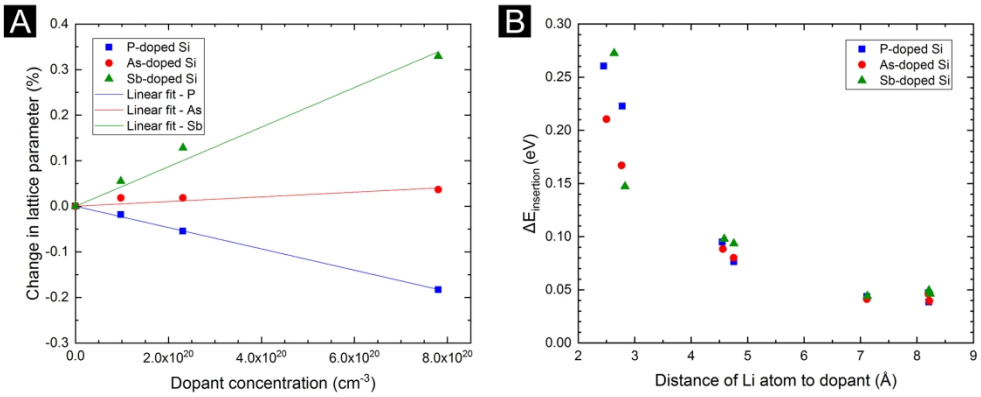

Figure 2: (A) Change in Si lattice parameter, computed using DFT, due to the introduction of P (■), As (●) and Sb (▲) dopants of increasing concentration into the crystalline Si lattice. (B) Relative change in Li insertion energy calculated for a Li ion inserted an increasing distance from a P, As or Sb dopant in a Si supercell comprising 216 atoms.

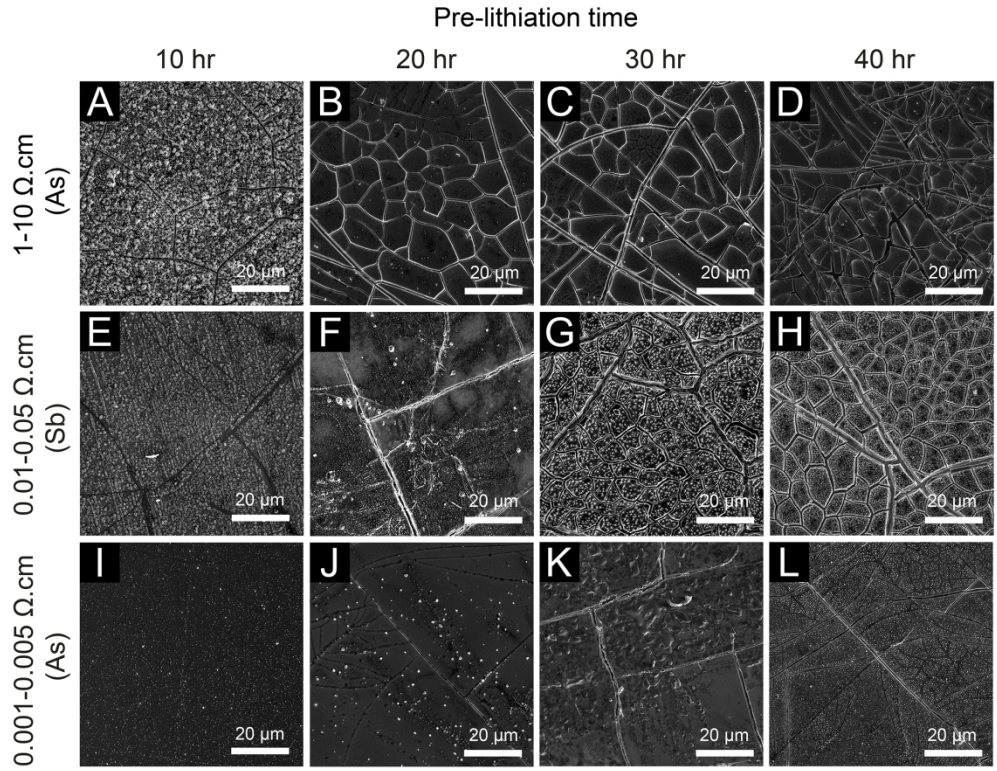

Figure 3: Scanning electron microscope images of the surfaces of selected 1–10 Ω cm As-doped (A-D), 0.01–0.05 Ω cm Sb-doped (E-H) and 0.001–0.005 Ω cm As-doped (I-L) Si anode. Si electrodes with different dopant densities were imaged after being prelithiated at 0.05 mA cm^{-2} for 10, 20, 30 and 40 hrs and then delithiated at the same current density to 3.0 V. The coin cells were then opened in a glove box, rinsed thoroughly with DMC and maintained under Ar until imaged. Higher magnification SEM images of the same Si electrodes are available in Figure S5.

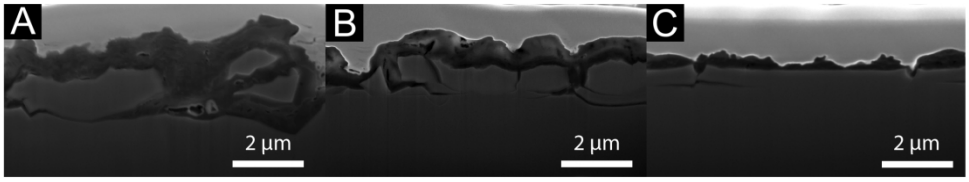

Figure 4: Cross-sectional SEM images recorded for selected 1–10 Ω cm As-doped (A), 0.01–0.05 Ω cm Sb-doped (B) and 0.001–0.005 Ω cm As-doped (C) Si electrodes which had been pre-lithitated for 10 hrs at 0.05 mA cm^{-2} and then discharged to 3.0 V prior to imaging. The surface of all electrodes was coated with Pt before imaging for increased conductivity.

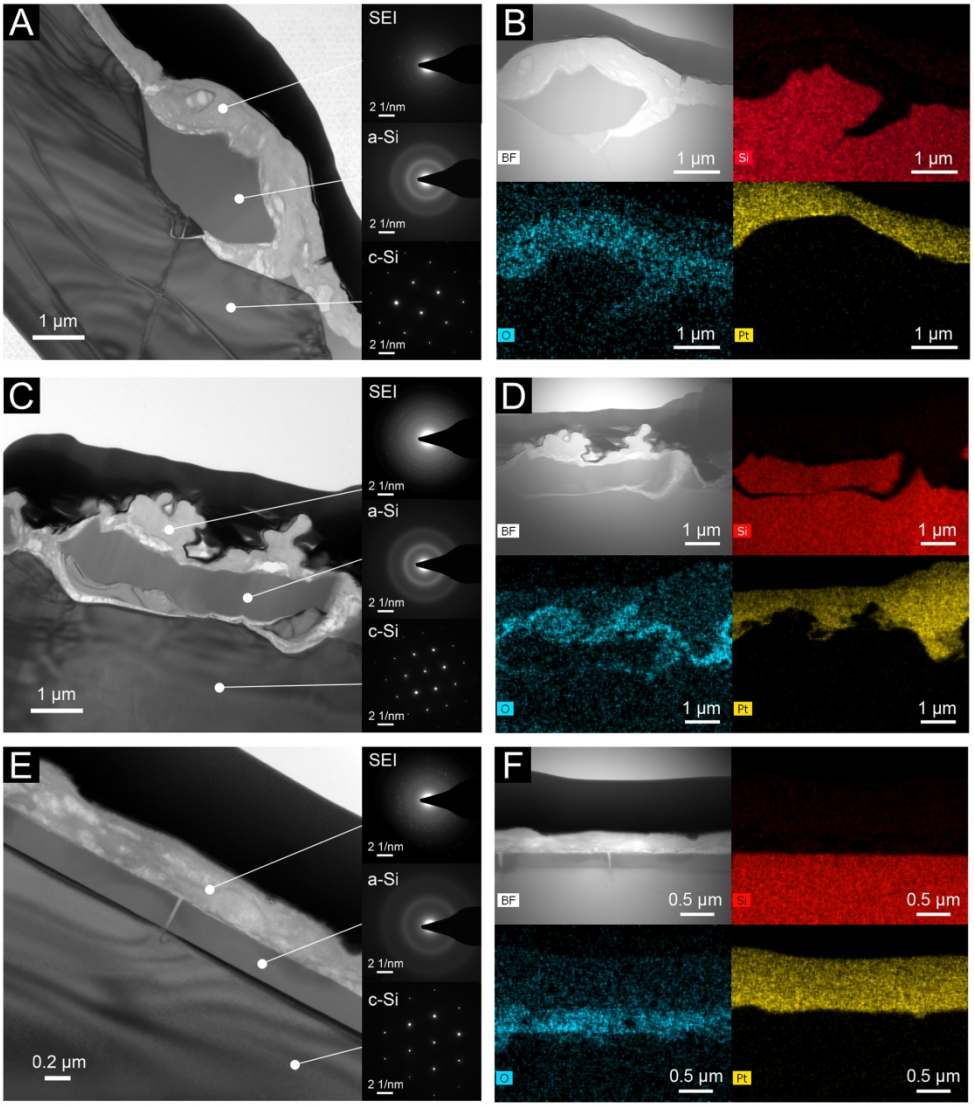

Figure 5: High resolution TEM cross-sectional images with SAED images (insets) and TEM-EDX analysis for Si electrodes of different doping density after prelithiation for 10 hr at 0.05 mA cm^{-2} and then discharging to 3.0 V prior to imaging; (A-B) 1–10 Ω cm As-doped, (C-D) 0.01–0.05 Ω cm Sb-doped and (E-F) 0.001–0.005 Ω cm As-doped Si electrodes.

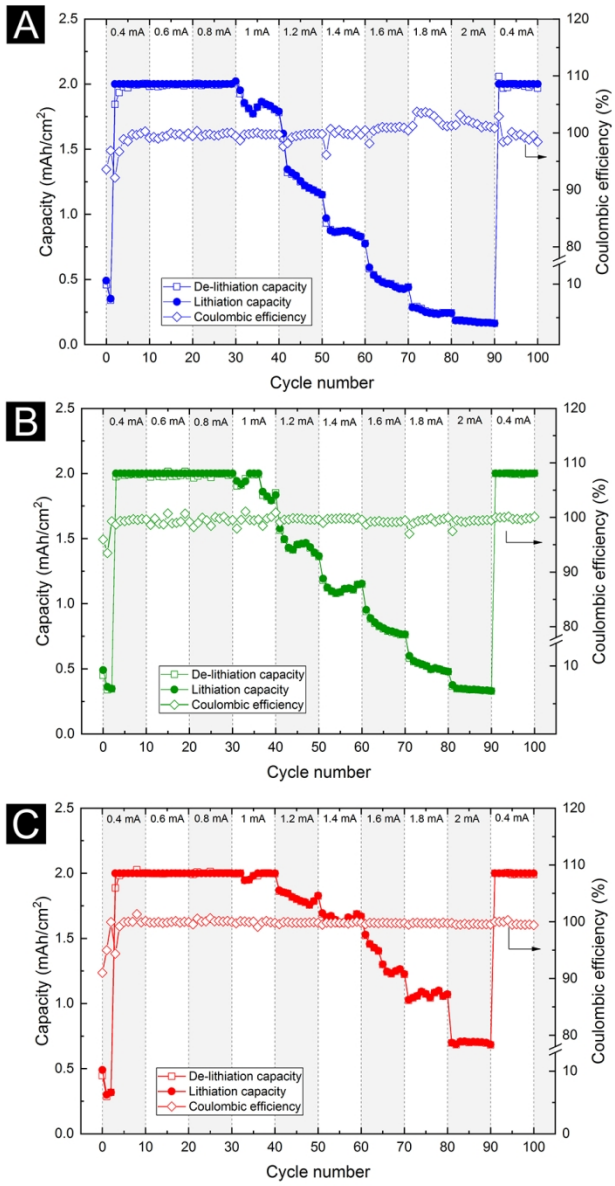

Figure 4: Cross-sectional SEM images recorded for selected 1–10 Ω cm As-doped (A), 0.01–0.05 Ω cm Sb-doped (B) and 0.001–0.005 Ω cm As-doped (C) Si electrodes which had been pre-lithitated for 10 hrs at 0.05 mA cm^{-2} and then discharged to 3.0 V prior to imaging. The surface of all electrodes was coated with Pt before imaging for increased conductivity.

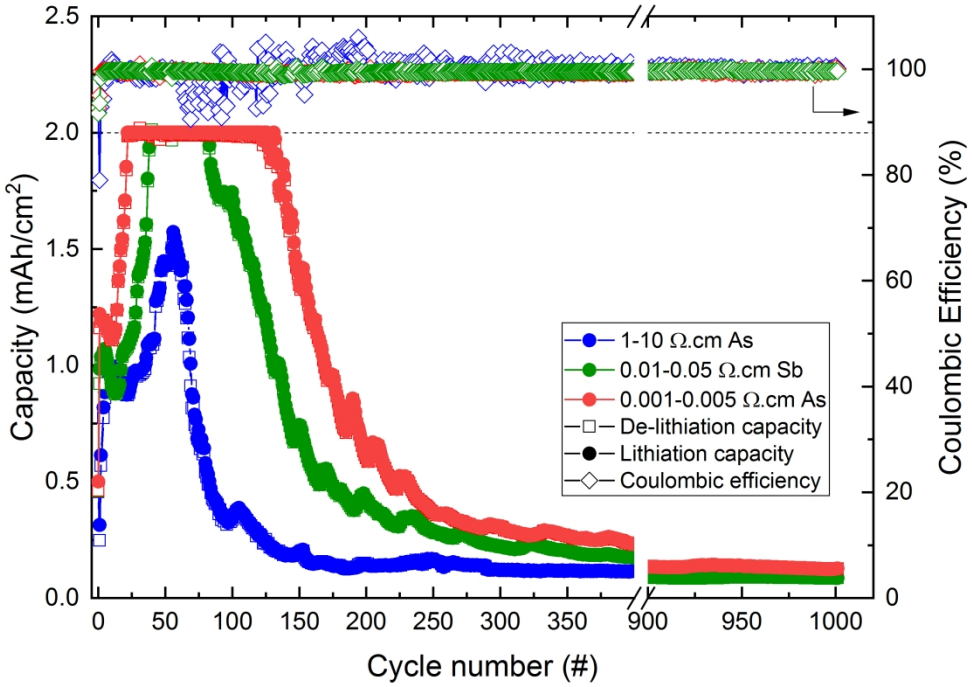

Figure 7: Lithiation/delithiation capacity and CE as a function of cycle number for representative 10 Ω cm As-doped (blue), 0.01–0.05 Ω cm Sb-doped (green) and 0.001–0.005 Ω cm As-doped (red) Si electrodes. All electrodes were prelithiated then cycled 1000 times at 1 mA cm^{-2} between 0.01–1.5 V with a capped capacity of 2 mAh cm^{-2}. An expanded view of the first 50 cycles can be found in the supporting information Figure S12.

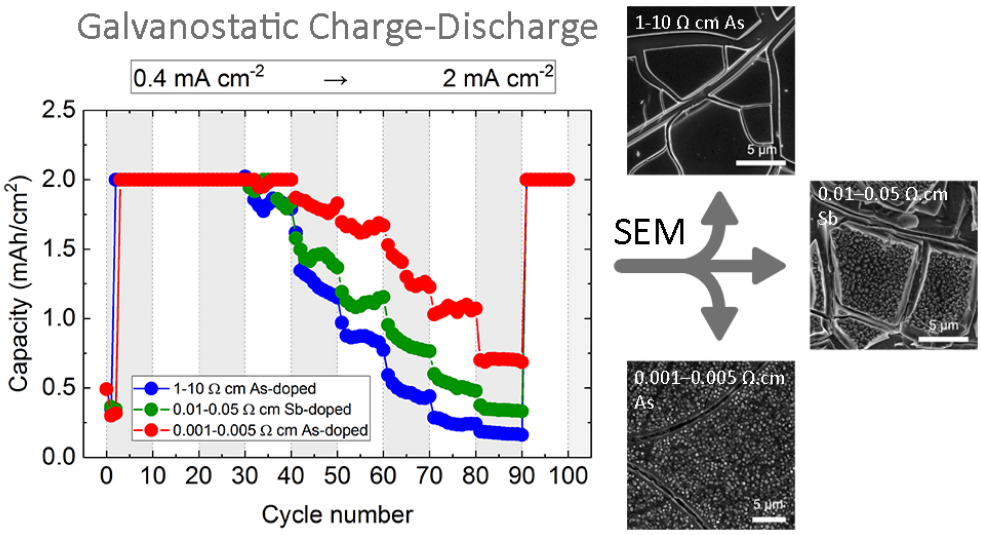
Galvanostatic Charge-Discharge
0.4 mA cm-2 → 2 mA cm-2
Capacity (mAh/cm2)
Cycle number
1-10 Ω cm As-doped
0.01-0.05 Ω cm Sb-doped
0.001-0.005 Ω cm As-doped
SEM
1-10 Ω cm As
0.01–0.05 Ω.cm Sb
0.001–0.005 Ω.cm As
5 µm